Nanoscale

Accepted Manuscript

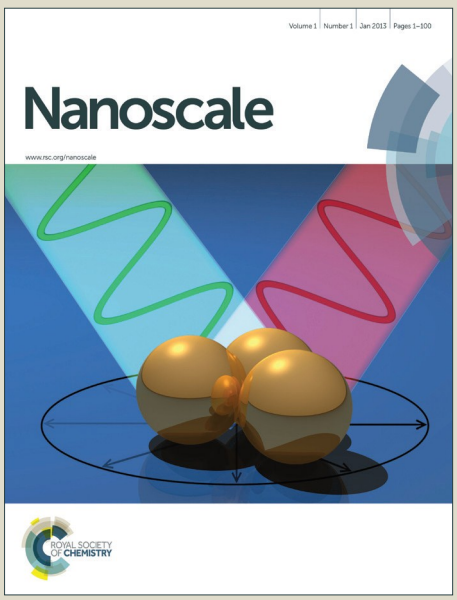

ROYAL SOCIETY OF CHEMISTRY

www.rsc.org/nanoscale

Extraordinary Optical Transmission in Nanopatterned Ultrathin Metal Film without Holes

Akshit Peer[1,3] and Rana Biswas*[,1,2,3]

[1]Department of Electrical and Computer Engineering, and [2]Department of Physics and Astronomy, Iowa State University, Ames, Iowa 50011, USA

[3]Ames Laboratory, Ames, Iowa 50011, USA

*Corresponding Author: biswasr@iastate.edu

ABSTRACT

We experimentally and theoretically demonstrate that a *continuous* gold film on a periodically textured substrate exhibits extraordinary optical transmission, even though no holes were etched in the film. Our film synthesis started by nanoimprinting a periodic array of nanocups of period ~750 nm on a polystyrene film over a glass substrate. A thin *non-conformal* gold film was sputter-deposited on the polystyrene with angle-directed deposition. The gold film was continuous with spatial thickness variation, the film being thinnest at the bottom of the nanocup. Measurements revealed an extraordinary transmission peak at a wavelength just smaller than the period, with an enhancement of ~2.5 as compared to the classically expected value. Scattering matrix simulations model well the transmission and reflectance measurements when an ultrathin gold layer (~5 nm), smaller than the skin depth, is retained at the bottom of the nanocups. Electric field intensities are enhanced by >100 within the nanocup, and ~40 in the ultrathin gold layer causing transmission through it. We show a wavelength red-shift of ~30 nm in extraordinary transmission peak when the nanocups are coated with a thin film of few nanometers, which can be utilized for biosensing. The continuous corrugated metal films are far simpler structures to observe extraordinary transmission, circumventing the difficult process of etching the metal film. Such continuous metal films with ultrathin regions are simple platforms for non-linear optics, plasmonics, and biological and chemical sensing.

INTRODUCTION

The seminal discovery of extraordinary transmission in sub-wavelength hole arrays by Ebbesen et al.[1] spurred an immense body of activity in sub-wavelength optics[2,3], plasmonics[4,5] and sensing[6,7]. It is very well established that a sub-wavelength array of holes in a free standing thin metal film, exhibits an extraordinary transmission peak at a wavelength (λ) close to array period (a) i.e. $\lambda \sim a$. When the hole array in the metal film resides on a substrate of refractive index n, there is an is an additional transmission peak at the wavelength $\lambda \sim na$. At both peaks the transmission is dramatically enhanced over the expected classical value[8] for the area of holes, with the enhancement increasing for smaller holes. The sub-wavelength holes do not allow transmission of classical waveguided modes. Rigorous studies established that the excitation of surface plasmon modes on both surfaces of the metal film and their coupling to each other underlies the physics of the extraordinary transmission (EOT) phenomena[9].

Experimental demonstration of EOT has typically involved *complex* multistep lithographic processes on thin metal films, with two approaches. A common approach employed for *small area* hole arrays, typically less than $1mm^2$, is to utilize photolithography for patterning and reactive ion etching (RIE) or focused ion-beam (FIB) milling for etching the arrays on thin metal films on substrates[10,11,12,13]. The optical properties of such small scale structures can only be measured with microspectrophotometers. The microspectrophotometer is a complex setup combining optical microscope with a sensitive spectrophotometer, and is used to measure the optical spectra of small area samples such as hole arrays[14,15] and patterned structures[16,17] non-destructively. The reflected, transmitted, or emitted light from the sample is collected either by the objective lens of the microscope or through optical fibers and focused on the spectrophotometer aperture for measurement. The microscope can be integrated with spectrophotometer to do measurement in UV-Vis-NIR region or infrared region (FTIR microscopy).

Alternatively patterning can be achieved by optical lithography performed with an elaborate projection lithography procedure, utilizing ultraviolet exposure, where a pattern on a reticle can be reduced (e.g. by a factor ~4) and transferred to photoresist, followed by reactive ion-etching to produce hole arrays[18]. In either case the fabrication involves advanced microelectronics facilities and procedures, and is difficult to implement for larger area samples. Previously metal

coated self-assembled polystyrene spheres[19] exhibited transmission peaks due to waveguide modes within the photonic crystal slab, but these experiments relied on fabrication of self-assembled monolayers.

We demonstrate a particularly simpler method to fabricate a subwavelength array structure using simple soft-lithographic procedures that does not require any nanofabrication facilities, and may be easily achieved in a workbench without high vacuum facilities. Moreover we demonstrate that a simple deposition of *continuous* metal film on a patterned substrate can exhibit EOT phenomena, without the need for etching features in the metal film – which is a particularly complex step. It seems counterintuitive that there are no holes in our deposited films, but the EOT relies instead on thickness variations of the metal film.

EXPERIMENTAL

Fabrication: The corrugated metal films were fabricated by the steps schematically depicted in Fig. 1a. We started with a master pattern (Microcontinuum Inc.) consisting of a periodic array of tapered nanocups (radius ~ 250 nm) with sub-micron period (~750 nm) patterned on a polycarbonate substrate by lithographic techniques, and a roll-to-roll process. Such master patterns and imprint stamps at customizable period and nanocup depth can also be commercially purchased from vendors[20], without the need for in-house nanofabrication. The inverse of this pattern on polycarbonate was transferred to a polydimethylsiloxane (PDMS) mold by soft lithography techniques[21] (*see PDMS Mold Preparation*). We used the patterned PDMS surface to transfer the pattern onto polystyrene (PS) films by first spin-coating PS films on a glass substrate and then imprinting the PS film with the PDMS mold, under elevated pressure and temperature (*see Polystyrene Film Preparation and Nanoimprinting*). Polystyrene is an excellent choice for the substrate since it is optically very well matched to the glass. Large area hole arrays have been fabricated by similar soft lithographic methods for enhanced thin film solar cells[22].

The patterned PS films were then sputter-coated (Denton, Desk V HP) with gold. We initially coated ~3nm iridium on the samples to increase the adhesion of thin gold layers on PS films. For sputtering the films, glass slides with the nanopatterned films were positioned at ~45° from the horizontal in the sputter chamber and rotated along the vertical axis so as to obtain highly non-

conformal coating over the nanocup arrays (Fig. 1a). This procedure is especially effective in coating the sidewalls of the arrays such that the metal coating is thicker at the top of the sidewall (~100 nm) and gradually becomes thinner as we move towards the bottom of nanocup sidewall (Fig. 1b). The bottom of the nanocup has an ultrathin gold coating (estimated at ~5 nm) that is smaller than the skin depth of gold ($\frac{\lambda}{2\pi Im(n)}$ ~ 25-30 nm) at optical wavelengths. Our deposition process ensures that the gold films are continuous. No further etching of the films was performed.

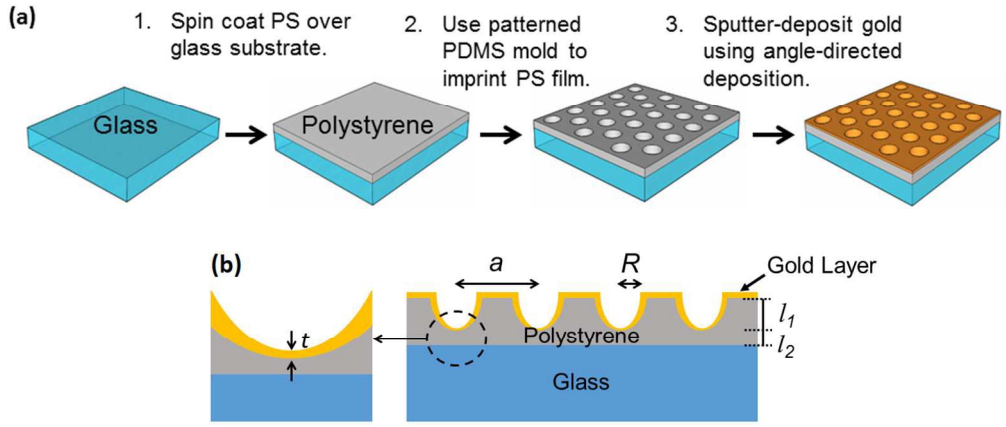

Figure 1. (a) Schematic illustrating imprinting the tapered nanocups on spin-coated polystyrene over glass substrate and subsequent gold deposition. (b) Cross sectional view of the gold-coated imprinted polystyrene surface with tapered nanocups. The magnified view of the encircled region is shown in left. The thickness of ultrathin gold layer at the bottom of the nanocup is t. l_1 is the imprint depth and l_2 is the thickness of polystyrene between the nanocup and glass substrate.

PDMS Mold Preparation: PDMS was prepared by mixing the elastomer base and curing agent (Sylgard 184, Dow Corning) in 10:1 w/w ratio. The mixture was degassed to remove any air bubbles. The mixture was then poured directly onto the master substrate with nanopatterns. After curing at room temperature for ~48 hours and subsequent heating on a hotplate at 65°C for ~12 hours, the PDMS was peeled off from the master substrate to expose the inverse pattern on the PDMS surface. The transferred pattern was characterized by scanning electron microscopy (SEM).

Polystyrene Film Preparation and Nanoimprinting: For preparing the PS films, polystyrene (Sigma Aldrich, average MW 35,000) was dissolved in toluene to form solutions with 2%, 5%

and 10% w/v concentration. The PS solution with different concentrations was spin-coated on the glass substrate (500 rpm, 60 seconds) to form thin films of different thicknesses, varying from 0.26 μm to 9 μm (Table 1). After allowing the films to dry for ~12 hours, the PDMS stamp was placed on each of the PS films over the glass substrate so that the patterned PDMS stamp faces the PS film. The PDMS stamp was further pressed down by another glass slide having the same size as substrate, and the assembly was held together with two binder clips at each end. The whole assembly was placed on a hotplate at 165°C, a temperature higher than the glass transition temperature (T_g) of PS (~100°C), for 45 minutes. After allowing it to cool at room temperature for 12 hours, the PDMS stamp was removed carefully from the PS films to reveal the inverse replica of the pattern on it. The thickness of the films obtained after spin-coating different concentrations of PS solution was measured using a Filmetrics F20 thin-film thickness measurement. The patterned nanocup array on PS films was characterized using SEM. All the samples were sputtered with ~3 nm iridium before SEM.

RESULTS AND DISCUSSION

Film Characterization: For solutions of concentrations 2%, 5%, and 10%, the measured film thicknesses were 0.265 ± 0.002 μm, 0.839 ± 0.012 μm, and 2.245 ± 0.041 μm, respectively. The measured PS film thicknesses were consistent with the data reported elsewhere[23]. The thickness of films over the glass substrate with different concentrations of PS solution is listed in Table 1.

Table 1. Thickness of polystyrene films for solutions of different concentrations.

Concentration (w/v)	Thickness (μm)
2%	0.265 ± 0.002
3%	0.369 ± 0.002
4%	0.569 ± 0.009
5%	0.839 ± 0.012
10%	2.245 ± 0.041
20%	9.014 ± 0.052

Figure 2a-c shows the SEM images of the patterned PS films for 2%, 5%, and 10% solution concentrations, respectively. The images show the regular array of tapered nanocups with a period of ~750 nm. The images demonstrate that the radius (R) of cups at the surface of the film fabricated using 2% PS solution is the smallest, and as a result the inter-cup spacing is largest. The nanocup radius increases and the depth decreases as the PS solution concentration increases from 2% to 10%. This yields three films with the same period (a) but different radius to period (R/a) ratio. The difference in R/a and nanocup imprint depth (l_1) can be ascribed to difference in film thickness and PS concentration – the 2% PS film is thin (~265 nm) and thus the stamp cannot penetrate completely into the film to replicate exactly the same radius of features as is on the stamp. However, at the same time, the stamp also has difficulty penetrating deep into the higher concentration PS film predominantly resulting in shallower features as the PS concentration increases from 2% to 10%.

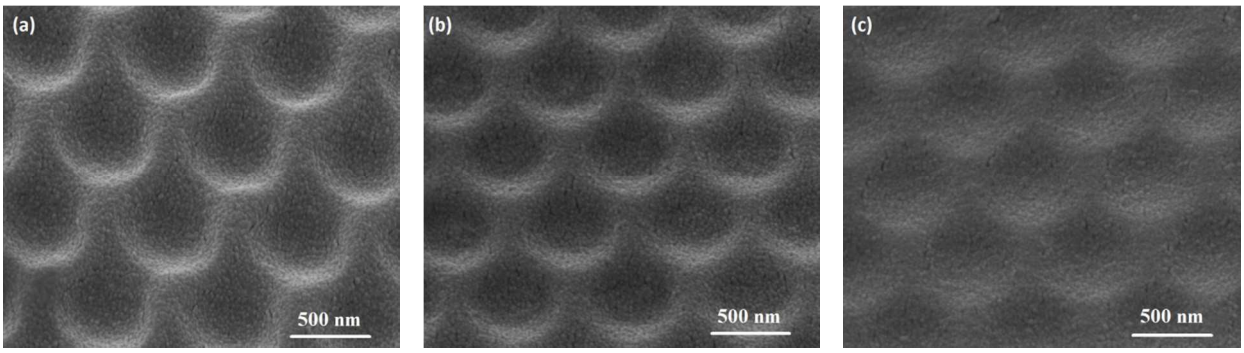

Figure 2. SEM micrographs of (a) 2%, (b) 5%, and (c) 10% w/v polystyrene films after nanoimprinting with PDMS stamp at a 45° tilt. All the films show tapered nanocups with period ~750 nm. The scale bar is 500 nm.

Optical Measurements: *Specular* transmission measurements on the gold-coated samples were performed using a Cary 5000 UV-Vis-NIR spectrophotometer, using an unpolarized source. The measured transmission characteristics of the gold-coated nanocup films (PS concentration 2%, 5%, 10%) are illustrated in Figure 3a-c. The strongest peak at λ_{sp} ~ 504 nm, present in all cases, corresponds to the characteristic surface plasmon resonance (SPR) peak of gold, which is expected at the wavelength when $|\varepsilon_{Au}+2\varepsilon_{air}|=0$[24]. The extraordinary transmission (EOT) peak remarkably appears at an expected λ_1 ~ 704 nm, nearly the period (a) of the structure. For nanocups on gold-coated 2% PSF (Fig. 3a), the transmission approaches ~4%, which is more than 2 times larger than the classically expected value. The enhancement factor of 2 is typical for EOT measurements, and the classic measurements of Ebbesen et al. also observed an

enhancement factor of 2-3 relative to the classically expected values. There is a weak transmision peak (T ~ 1.5%) at ~1000 nm which gradually diminishes as the concentration of PS solution increases. This peak appears at a wavelength $\lambda_2 \sim an_0$, where n_0 is the refractive index of the glass substrate ($n_0 \sim 1.5$). As expected, the EOT peak becomes weaker as the PS solution concentration increases from 2% to 10%, corresponding to decrease in depth of the nanocup.

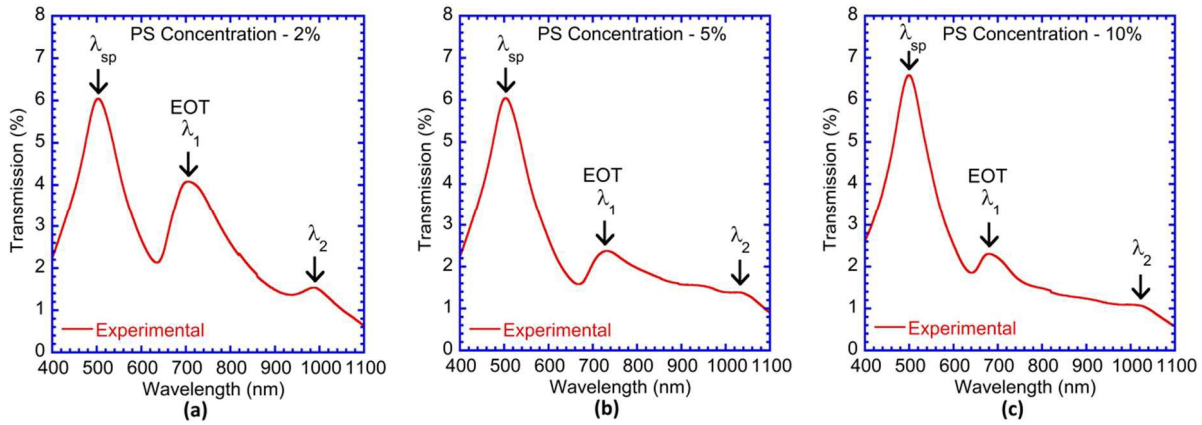

Figure 3. Measured transmission spectra of gold-coated polystyrene films with (a) 2%, (b) 5%, and (c) 10% concentration. The peak at $\lambda_{sp} \sim 504$ nm corresponds to SPR peak of gold. The peak at $\lambda_1 \sim 704$ nm is the EOT peak.

Surface Plasmons: Our experimental EOT peak and the simulated results (described in next section) support the formation of surface plasmons (SPs) on the periodically corrugated nanocup lattice. To see this connection, we note that the triangular lattice (with period a) has the reciprocal lattice vectors $\boldsymbol{G}$:

$$G_1 = \frac{2\pi}{a}(1, -\frac{1}{\sqrt{3}}); G_2 = \frac{2\pi}{a}(0, \frac{2}{\sqrt{3}}) \quad (1)$$

Surface plasmons at metal-dielectric interface films are longitudinal modes propagating along the surface with exponentially decaying amplitude away from the interface, with the dispersion relation,

$$k_{sp} = \frac{\omega}{c}\left(\frac{\varepsilon_1 \varepsilon_2}{\varepsilon_1 + \varepsilon_2}\right)^{1/2} \quad (2)$$

k_{sp} is the wave-vector of surface plasmons and ω is the angular frequency. ε_2 is the real part of the metal dielectric function that is negative, and large in magnitude, for IR frequencies. ε_1

describes the dielectric media. Since the surface plasmon dispersion lies below the incoming light line for any angle of incidence (θ), incoming light cannot directly generate SPs on a smooth surface.

When an incident light of angular frequency ω, impinges on the patterned surface at an angle θ, it can couple to a surface plasmon at the air-metal interface through a reciprocal lattice vector,

$$\frac{\omega}{c}\sin\theta\,\mathbf{i}+\mathbf{G}=\mathbf{k}_{sp} \tag{3}$$

By combining the dispersion relation (2) with the momentum conservation condition (3), we get the well-known eigenvalue equation for the surface plasmon frequencies,

$$\left(\frac{\varepsilon_1\varepsilon_2}{\varepsilon_1+\varepsilon_2}\right)=\left(\sin\theta\cos\varphi\pm i\frac{v_0}{v}\right)^2+\left(\sin\theta\sin\varphi\mp i\frac{1}{\sqrt{3}}\frac{v_0}{v}\pm j\frac{2}{\sqrt{3}}\frac{v_0}{v}\right)^2 \tag{4}$$

Here the dimensionless frequency unit is v_0=c/a (400 THz for a=750 nm). The fundamental mode (i=1, j=0 or i=0, j=1), or Wood's anomaly, is predicted to occur at $\lambda_W=\sqrt{3}a/2$, i.e. at a wavelength slightly *smaller* than the lattice period a, for the triangular lattice symmetry. At this wavelength $\lambda_W=\sqrt{3}a/2=0.866a$ (650 nm for a=750 nm) the transmission T has a minimum, and is the position of the well-known Wood's anomaly, where the diffraction order changes from evanescent to propagating. The EOT peak occurs at a wavelength λ_1 slightly larger than this value near ~704 nm (Fig. 3), which is still slightly smaller than the period a. The wavelength difference between the EOT peak and the Wood's anomaly depends on details of the metal layer thickness, hole radius, and geometry. λ_1 is close to a and can be slightly lower/higher than a depending on the geometry.

It is interesting to compare this analysis with the more frequently used square lattice, where the Wood's anomaly is predicted to occur at a wavelength of a, where T=0, and the EOT peak is at a wavelength slightly *larger* than a. This is precisely the result which we found in our previous scattering matrix simulations for the square lattice[26], where the minimum T occurs at $\lambda \sim a$ and the EOT peak at $\lambda > a$ (square lattice).

Optical Simulations: We use the rigorous scattering matrix (SM) method[25] to simulate the electromagnetic properties of subwavelength nanocup arrays on a gold-coated polystyrene film and understand the underlying physics. The simulated structure is similar to that Fig. 1a with tapered nanocup arrays arranged in triangular symmetry in the lattice. The simulation

methodology for similar structure has been described in detail in our previous publications[26,27]. Briefly, Maxwell's equations are solved in Fourier space in three-dimensions. The structure is divided into slices along the *z*-axis and the dielectric function $\varepsilon(r)$ is expressed as a periodic function of the planar coordinates (*x*,*y*) in each slice. Hence the dielectric function and its inverse are expressed as a Fourier expansion with coefficients $\varepsilon(\mathbf{G})$ or $\varepsilon^{-1}(\mathbf{G})$, where **G** are the reciprocal lattice vectors of the two-dimensional lattice. The electric and magnetic fields are expanded in Bloch waves, N_G (*k* is a Bloch wave vector).

$$\mathbf{E}_{\mathbf{k}}(\mathbf{r}) = \sum_{\mathbf{G}} \mathbf{E}_{\mathbf{G}}(z)\, e^{i(\mathbf{k}+\mathbf{G}).\mathbf{x}_{||}} \tag{5}$$

A transfer matrix in each layer is calculated that relates the *z* dependence of the **E**, **H** fields in each layer. The transfer matrix includes both polarizations of the wave, and is diagonalized to obtain the eigenmodes within the layer. Continuity of the parallel components of **E** and **H** at each interface leads to the individual scattering matrices of each layer, which are then convoluted into the scattering matrix S for the entire structure using a recursion algorithm. Using the total S matrix, we obtain the reflection and transmission of the structure when fields are incident from the top. For this case, we have tested the convergence of these results with 400-769 Bloch waves (N_G) per polarization corresponding to a scattering matrix size of 800-1538 (Section III, ESI). The number of Bloch waves terminates on a closed shell of reciprocal lattice vectors **G**. The largest scattering matrix of 1538 cannot be performed easily with routine compilation due to memory constraints and requires dynamic linking of runtime libraries[28]. The convergence was achieved with ~535-769 Bloch waves corresponding to scattering matrix size of 1070-1538 for both polarizations of the field in the triangular lattices (Fig. S4, ESI)[26]. We utilize the experimentally measured frequency dependent dielectric functions $\varepsilon(\lambda)=(\varepsilon_1,\varepsilon_2)$ of gold[29].

The physics underlying the SM matrix method is very similar to that employed in the rigorous coupled wave analysis (RCWA), where the fields are expanded also in Bloch waves. Early RCWA simulations[30,31] have concentrated on 1-d grating structures, where TE and TM modes are decoupled. Most implementations of RCWA utilize a transfer matrix to connect the fields in one layer with the next successive layer, utilizing continuity of the parallel components of **E** and **H**. The transmitted and reflected fields are obtained through transfer matrices on each layer. The SM utilizes the individual scattering matrices s_i for each layer which can have greater stability

than the transfer matrices.[32] Rather than computing the fields at the individual layers in RCWA, the entire scattering matrix of the structure is computed in SM.

We plot the computed transmission spectra for gold-coated polystyrene films in Figs. 4a and 4b, in conjunction with measurements. Similar to the experimental geometry for the film fabricated from 2% PS solution, the simulations have been done for array of nanocups arranged in a triangular lattice of period (a) 750 nm (see Section I, ESI for simulations with different values of a and R/a). The polarization is along the x-axis – the symmetry of the nanocups. Due to triangular lattice symmetry all polarizations rotated by 60° from the x-axis, and polarization vectors reflected through the six mirror planes are equivalent at normal incidence. The nanocups are tapered with largest R/a ~ 0.33 at the surface and the smallest R/a ~ 0.06 at the bottom rendering the nanocups highly subwavelength as their depth from the surface increases (Fig. 1b). Simulations utilized different thickness (t) of an ultrathin gold layer between the substrate and the nanocup as shown in Fig. 1b.

It can be seen that the computed transmission spectra for (Figs. 4a,b) for two different thicknesses of the ultrathin gold layer (t = 5 nm, 10 nm) are in reasonable agreement with the measured values, especially for the positions and magnitudes of the transmission peaks. The simulated transmission shows a doublet peak at 707 nm and 720 nm centered at the same wavelength as the measured curve (Fig. 4a). There are additional sharp side-bands on both sides of the simulated doublet peak. It is expected that these features will combine into the single broad peak observed in experiment at 704 nm. Furthermore, averaging over all the polarizations in the plane also results in the generation of a broader peak centered at 704 nm. The EOT peak occurs from the generation of surface plasmons at the top surface of the structure – the corrugated air-gold interface – as discussed previously. There is a second weaker SP at the gold-(PS/glass) interface at $\lambda_2 \sim n_0 a \sim 1.5a$ near ~1.0 μm. The interaction between the gold-air and gold-(PS/glass) SPs splits each of them into double modes similar to a SP molecule[9] with the splitting dependent on the spatial separation between the two interfaces. This is the cause of the double peak feature at 707-720 nm and also the weaker double peak at 950-1000 nm (visible more clearly as a reflectance dip in Fig. 4c). The simulated transmission is smaller than experiment because the experimental structure has gold sidewalls that are gradually graded from the thin value (5-10 nm) to the bulk value, whereas the simulations assume a fixed thickness of

gold on the sloping sidewalls, thereby overestimating the gold content and reducing the transmission. Another notable feature (Figs. 4a,b) is the departure of the simulated specular transmission (T_{spec}) from the total transmission (T_{tot}) at the expected Wood's anomaly wavelength $\lambda_W=\sqrt{3}a/2=$ 660 nm when the incoming wave-vector ($k=2\pi/\lambda$) matches the first reciprocal lattice vector ($G_1=2(2\pi)/\sqrt{3}a$). Below this wavelength diffraction takes place and decreases the specular transmission (described in previous section on *Surface Plasmons*). This is exactly the case for the simulations where $T=0$ at $\lambda_W=660$ nm (Fig. 4a), and the measured T has a minimum at ~635 nm.

The various features of the transmission spectra (Fig. 4a) are also represented in the reflectance (Fig. 4c). The simulated and measured transmission peaks at 504 nm from the gold surface plasmons correspond to broad regions of low reflectance below 510 nm. At short wavelengths near 400 nm the structure is absorbing and has low T and R. The simulated EOT peak at ~707 nm corresponds to a sharp minima of the reflectance (R~0, Fig. 4c). Similarly, the experimental EOT peak at 704 nm corresponds to the measured reflectance minimum at ~725 nm. The two weak double peaks in the simulated T at 950 nm and 1000 nm also appear as distinct shallow reflectance minima. The Wood's anomaly related minima in T at ~660 nm (simulation) and 635 nm (experiment) correspond to the maxima in simulated and experimental reflectance, at similar wavelengths. The simulated reflectance is overall somewhat higher than measurement possibly due to the random fine grain gold structure (<50 nm) seen in the SEM (Fig. 2), that is superimposed on the larger scale periodicity, and may cause additional scattering in the experimental structure.

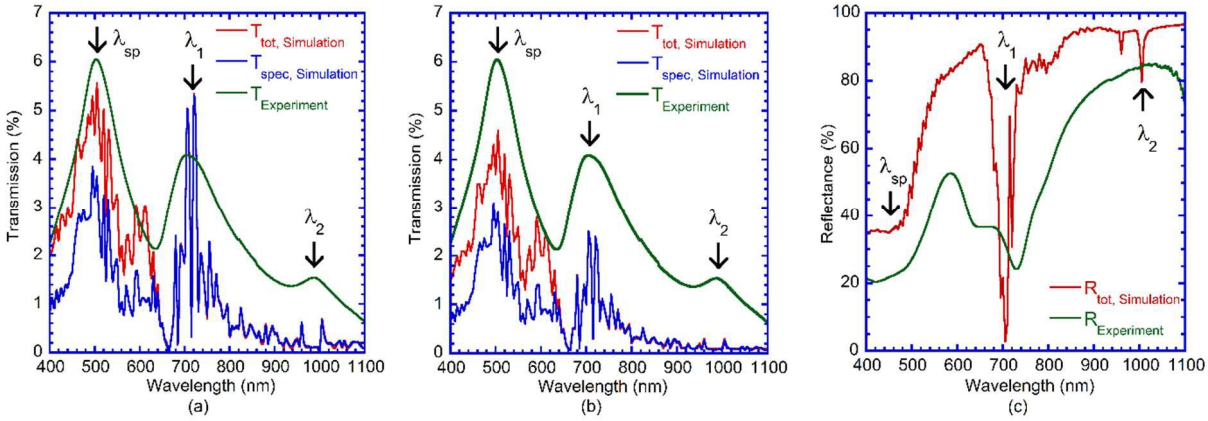

Figure 4. Simulated transmission through tapered nanocup array arranged in a triangular lattice of period 750 nm for two thicknesses (t) of the ultrathin gold layer (a) 5 nm, and (b) 10 nm at the bottom of the nanocup. The simulations are done for constant R/a = 0.33 at the nanocup opening. (c) Comparison of simulated (red) total reflection spectra with experimental (green) values for 2% concentration gold-coated PS film, for the 5 nm ultrathin gold film. The simulations utilize N_G=769.

The multi-layered experimental structure is more complex consisting of nanocup / Au (5 nm) / Ir (3 nm) / PS (15 nm) / Glass. The PS thickness below the nanocup is the thickness of the starting PS layer (265 nm for 2% solution - Table 1), from which the experimentally determined imprinted depth ($l_1 \sim 250$ nm) is removed, resulting in $l_2 \sim 15$ nm of PS between the nanocup and glass substrate (see Fig. 1b). We have simulated the effect of this multilayer structure that adds a 3 nm Ir layer and the PS layer of index n_{PS} = 1.57 between the Ir and the glass. The resulting transmission shown in Fig. 5 (lower panel) is not significantly affected from the result in Fig. 4a (also Fig. 5, upper panel), showing both the gold SP peak and the EOT peak at the similar positions without the Ir or PS layer.

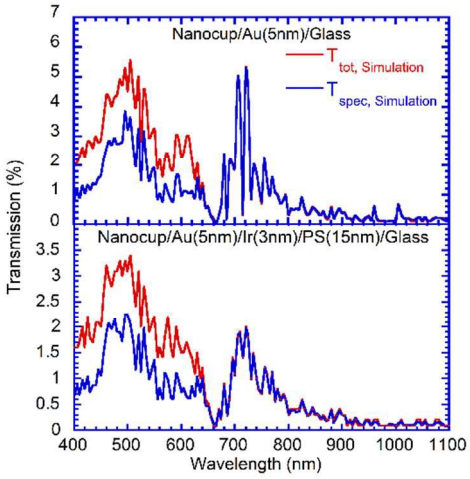

Figure 5. Simulated transmission through tapered nanocup array consisting of nanocup / Au(5 nm) / Ir(3 nm) / PS(15 nm) / Glass arranged in a triangular lattice of period 750 nm. The simulated transmission for nanocup / Au(5 nm) / Glass (same as Fig. 4a) is presented in the upper panel for comparison. The simulations utilize N_G=769.

Electric Field Intensity Profile: To obtain insight into the extraordinary transmission mechanisms we calculate the electric field intensity $|\mathbf{E}|^2$ at the resonant λ_1 = 700 nm in the xz-plane perpendicular to the structure and passing through the symmetry axis of the nanocup array (Fig. 6a). Within the air region of the nanocups very large field enhancements exceeding 100 are found, with the highest enhancements occurring in a layer ~40 nm above the bottom of the

nanocup, where modal maxima occur. Since the opening radius of the nanocup (R/a ~ 0.33) exceeds the waveguide cutoff for propagating modes (R/a ~ 0.29) in a cylindrical waveguide[33], the lowest order modes (such as TE_{11}, TM_{01}) can begin propagating in the upper region of the nanocup. As the nanocup tapers the mode gets squeezed near the bottom of the nanocup producing regions of high field intensity. Focusing of fields to high intensities near the bottom of a nanocone hole array in Si have also been observed in simulations[34]. We also show the transverse *xy*-plane field distribution right at the nanocup surface for λ_1 = 700 nm (Fig. S3, ESI) which confirms the field distribution of Fig. 6a (see details in Section II, ESI).

A magnified view of the ultrathin gold layer and substrate (Fig. 6b) shows very large electric field intensities within the 10 nm ultrathin gold layer, with intensities enhanced by a factor of 30-40 *inside* the gold layer. The field transmits through the ultrathin gold layer in a very narrow cylindrical profile of width ~50 nm, into the substrate, with the axis of the cylinder along the depth axis (*z*-axis). The cylindrical mode profile is deeply sub-wavelength with a spatial scale <λ/10. This is possible since the thickness of the ultrathin gold layer, is smaller than the skin depth of gold at optical wavelengths ($\frac{\lambda}{2\pi Im(n)}$ ~ 25-30 nm). The $|\mathbf{E}|^2$ is enhanced by 30-40 at the gold-glass interface and by >10 at a depth of ~20 nm in the glass. Such enhancements in the field intensity can lead to strong non-linear phenomena such as second harmonic generation (SHG)[35,36], which is proportional to the localized $|\mathbf{E}|^2$. Qualitatively, the transmission arises from a focusing of a waveguide mode into the ultrathin gold layer. The transmission peak at 504 nm is due to the surface plasmon mode of gold where $|\mathbf{E}|^2$ is enhanced by 3-4 within the nanocup (Fig. 6c) and the intensity is large at the entire gold-air surface. The SPP mode generates transmission through the ultrathin gold layer into the glass.

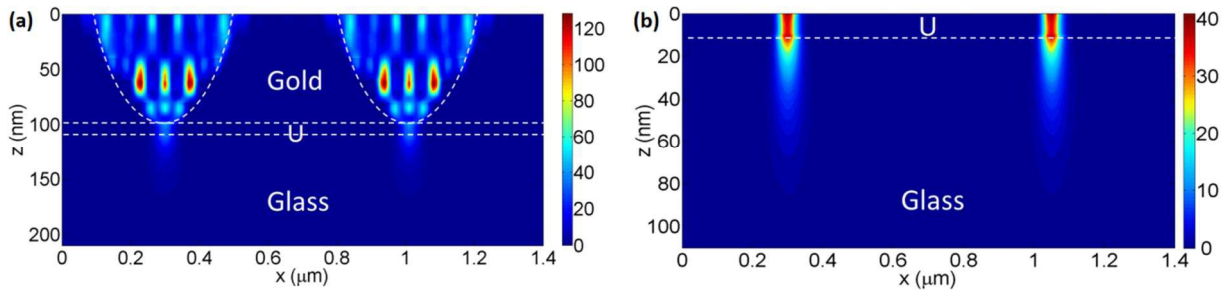

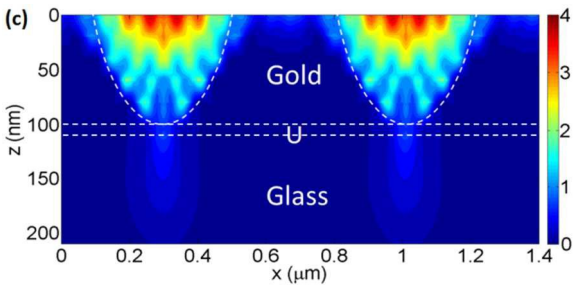

Figure 6. (a) Electric field intensity at λ_1 = 700 nm showing the enhanced field in the *xz*-plane. (b) Enlarged view of the electric field intensity plot showing the fields in glass and ultrathin gold layer (U). (c) Electric field intensity at λ_{sp} = 504 nm showing the enhanced field in the *xz*-plane.

Discussion: Previous observations of EOT have been performed on well-defined holes or cavities in metal films. We demonstrate that a *continuous* gold film deposited on a periodically corrugated substrate demonstrates the EOT, without the need to do any etching of the film. This result is counter-intuitive, and may be understood by recognizing that the thickness of our metal film is highly non-uniform. The sputter-deposition of gold at a 45° angle to the substrate likely generates thicker sidewalls within the nanocup arrays, and very thin gold coatings at the bottom of the conical pits (Fig. 1b), which may be comparable or less than the skin depth of gold (~25-30 nm at optical wavelengths). The thin non-uniform layer of gold at the bottom of the conical pits, may allow sufficient light transmission, whereas the thicker gold film away from the bottom of the conical pits will not allow light transmission. Our method does not require self-assembly of spheres[19]. Self-assembly results in domain formation and random point defects – both features causing larger inhomogeneities than in nanoimprinting method that we utilize here. Furthermore the transmission occurs through the ultrathin metal layer in our nanocup array in contrast to waveguided modes through the spheres in the self-assembled structure[19]. For a triangular lattice, the fraction of area occupied by nanocups in the film is given by $f = \pi R^2 \Big/ \left(\sqrt{3}a^2 / 2\right)$. For smallest R/$a$ ~ 0.06, f ~ 1.5%. We see that the transmission (T ~ 4%) is enhanced significantly by more than a factor of 2.5 compared to the fraction of the area occupied by nanocups in the film. The enhancement factor of 2.5 is typical of *larger* radius (R/a) arrays. It is well known that when the radius of the apertures decreases the enhancement factor increases considerably. For example at R/a=0.2 we found an enhancement factor of 8 in our previous work on hole arrays[26].

A continuous film also allows the possibility of modulating optical transmission in the presence of a current flow in the continuous gold film i.e. under current bias, where currents flow in the thin Au film region through which light transmits. Although currents can flow in discontinuous hole array films, there is no current flow within the holes, limiting electro-optical effects.

Thus our novel corrugated structure has the functionality of a subwavelength hole array *without* actually having holes or etched features, and can be replicated over large areas with continuous gold films. As noted earlier, the complex step of etching the film is no longer required, and advanced nanofabrication facilities are not necessary

Ultrathin Films: We note that recently there has been great interest in continuous ultrathin coatings, with thickness far smaller than the optical thickness. Highly absorbing dielectric coatings (of Ge) as small as 5-25 nm thickness exhibited novel interference effects which selectively absorb and transmit various wavelengths of visible spectrum[37]. Ultrathin silver coatings have been shown to have a reflection phase shift continuously tunable from a perfect electric mirror ($\varphi=\pi$) to a perfect magnetic mirror ($\varphi=0$) depending on the thickness of the coating[38]. This changes the standing wave profile in planar devices allowing highly enhanced absorption in sub-100 nm thick solar cell layers[38] – a feature not possible with conventional optically thick metal coatings. Our ultrathin gold film is an example of novel optical effects arising from ultrathin films, and illustrates surprising consequences of such optically thin films, that are of much topical interest.

Biosensing Applications: We envisage our nanocup structure may have robust application to biosensing, where a thin protein layer can be coated on the surface of the nanocup lattice. Experiments by Cetin[39] et al. with a bare gold nanohole square array (of period 600 nm and hole diameter 200 nm) demonstrated the typical EOT peak at 683 nm. After binding a protein bilayer of 3 nm thickness the EOT mode shifted to 702 nm, due to the minute changes in the refractive index in the vicinity of the nanohole. The wavelength shift was proportional to the protein (IgG) concentration, resulting a lens-free imaging platform with a detection limit of $\mu g\ ml^{-1}$. In these experiments *small* 100 μm x 100 μm pixels were utilized, fabricated with e-beam lithography.
We envisage our nanocup structure would serve as a robust platform for biosensing, utilizing far *larger* pixels upto and exceeding 1cm x 1cm in size. A protein bilayer few nm thick can bind on the nanocup surface, and result in a detectable shift of the EOT transmission peak at ~700 nm.

Furthermore our large area nanocup structure could be fabricated with much faster throughput and lower cost than with the traditional e-beam lithographic methods.

We illustrate this biosensing concept with a simulation of a thin biosensing film of thickness d, and a typical dielectric (protein) refractive index $n_{diel} \sim 1.4$ on the surface on the nanocup. Our simulations (Fig. 7 with $N_G = 535$) show a red-shift $\Delta\lambda$ of the EOT peak by 30 nm with a 5 nm coating, typical of a protein bilayer. An additional gold-dielectric surface plasmon transmission peak appears at $\sim n\lambda_1 \sim$ 800-830 nm corresponding to the average n (~1.2) of air and dielectric (protein) layer.

We note that the EOT based biosensing approach is in contrast to the local SP resonance (LSPR) methods extensively developed[40,41,42] utilizing functionalized gold nanoparticles that exhibit the LSPR peak dependent on the size and shape of the nanoparticle. When the analytes bind to the functional group, characteristic wavelength shifts ($\Delta\lambda$), as large as 20-67 nm, are readily observed[40]. A future direction may be to combine the nanoparticles with nanohole/nanocup arrays to detect biomolecules at even lower concentration.

Very recent studies have shown that such nanohole/nanocup arrays exhibiting EOT can be used for other novel biological and imaging applications. Silver nanohole arrays coated with various biological species were imaged with surface-enhanced Raman spectroscopy (SERS) and focused hotspots were positioned using holographic laser illumination[43], to produce a blinking behavior of the hotspots. Nanohole arrays in free standing metal-coated nitride films were used for trapping and analyzing single organelles such as mitochondria[44]. Similarly, binary nanohole structures having two different hole sizes and linear nanoguides were used for exciting fluorescence from bacterial species and observing bacterial dynamics with subwavelength precision[45].

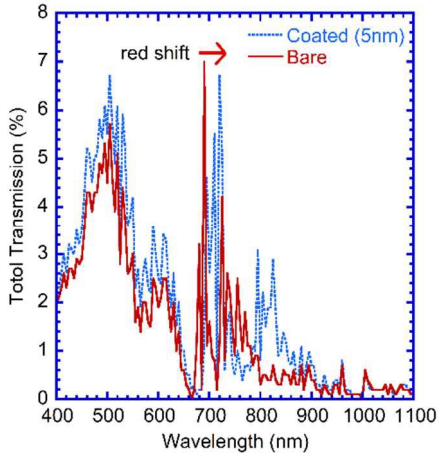

Figure 7. Simulated transmission for nanocup structure with and without a 5 nm adsorbed layer, illustrating the red-shift of the EOT peak by 30 nm. The simulations utilize N_G=535.

CONCLUSION:

In summary, we experimentally and theoretically demonstrated the extraordinary transmission on a *continuous* gold film deposited on periodically corrugated substrates, even though no holes were etched in the film. The varying thickness of the gold film on the corrugated substrate enables spatial regions of high transmission through ultrathin regions of the films (~5 nm) that are thinner than the skin depth, in conjunction with negligible transmission through thick regions of the metal film. This phenomenon has functionality similar to a nanohole array. Simulated fields show very high enhanced intensity (~40) in the ultrathin gold layer, and >100 within the nanocup. The extraordinary transmission peak is red-shifted by 30 nm when the nanocups are coated with a few nm thin analyte film, which can find applications in biosensing. Our procedure provides a simple, rapid, low-cost process to fabricate *large area* arrays where complex nanofabrication is not needed, but show the extraordinary transmission phenomena, observable in any spectrophotometer. Our corrugated continuous metal coated structures have much promise for photonics applications, without the need for microscopy in performing experiments.

ACKNOWLEDGEMENTS:

We thank Dr. J. Kim and R. Dhakal for assistance with soft lithography, and P. H. Joshi for transmission measurements. This research was partially supported by the National Science Foundation through Grant CMMI-1265844 (fabrication); and the Ames Laboratory, which is operated for the U.S. Department of Energy (USDOE) by Iowa State University under contract No. DE-AC02-07CH11385 (optical measurements and theoretical analysis). We acknowledge use of computational resources at the National Energy Research Scientific Computing Center (NERSC) which is supported by the Office of Science of the USDOE under Contract No. DE-AC02-05CH11231.

NOTES AND REFERENCES:

(1) T. W. Ebbesen, H. J. Lezec, H. F. Ghaemi, T. Thio and P. A. Wolff, *Nature*, 1998, **391**, 667–669.

(2) C. Genet and T. W. Ebbesen, *Nature*, 2007, **445**, 39–46.

(3) W. L. Barnes, A. Dereux and T. W. Ebbesen, *Nature*, 2003, **424**, 824–30.

(4) H. F. Ghaemi, T. Thio, D. Grupp, T. W. Ebbesen and H. J. Lezec, *Phys. Rev. B*, 1998, **58**, 6779–6782.

(5) W. L. Barnes, W. A. Murray, J. Dintinger, E. Devaux and T. W. Ebbesen, *Phys. Rev. Lett.*, 2004, **92**, 107401–1.

(6) T. Rindzevicius, Y. Alaverdyan, A. Dahlin, F. Höök, D. S. Sutherland and M. Käll, *Nano Lett.*, 2005, **5**, 2335–2339.

(7) Y. Liu, J. Bishop, L. Williams, S. Blair and J. Herron, *Nanotechnology*, 2004, **15**, 1368–1374.

(8) H. A. Bethe, *Phys. Rev.*, 1944, **66**, 163–182.

(9) L. Martín-Moreno, F. J. García-Vidal, H. J. Lezec, K. M. Pellerin, T. Thio, J. B. Pendry and T. W. Ebbesen, *Phys. Rev. Lett.*, 2001, **86**, 1114–1117.

(10) K. L. Van Der Molen, K. J. Klein Koerkamp, S. Enoch, F. B. Segerink, N. F. Van Hulst and L. Kuipers, *Phys. Rev. B*, 2005, **72**, 045421.

(11) Y. H. Ye and J. Y. Zhang, *Appl. Phys. Lett.*, 2004, **84**, 2977–2979.

(12) K. J. K. Koerkamp, S. Enoch, F. B. Segerink, N. F. Van Hulst and L. Kuipers, *Phys. Rev. Lett.*, 2004, **92**, 183901.

(13) T. Thio, H. F. Ghaemi, H. J. Lezec, P. A. Wolff and T. W. Ebbesen, *J. Opt. Soc. Am. B*, 1999, **16**, 1743.

(14) K. Kumar, H. Duan, R. S. Hegde, S. C. Koh, J. N. Wei and J. K. Yang, *Nature Nanotech.*, 2012, **7**, 557–561.

(15) V. Canpean and S. Astilean, *Lab Chip*, 2009, **9**, 3574-3579.

(16) R. H. Fan, L. H. Zhu, R. W. Peng, X. R. Huang, D. X. Qi, X. P. Ren, Q. Hu and M. Wang, *Phys. Rev. B*, 2013, **87**, 195444.

(17) Y. Liu, R. Dhakal, V. Dalal and J. Kim, *Appl. Phys. Lett.*, 2012, **101**, 233904.

(18) B. Curtin, R. Biswas and V. Dalal, *Appl. Phys. Lett.*, 2009, **95**, 93–96.

(19) L. Landström, D. Brodoceanu, D. Bäuerle, F. J. Garcia-Vidal, S. G. Rodrigo and L. Martin-Moreno, *Opt. Express*, 2009, **17**, 761–772.

(20) Benchmark Technologies, http://www.benchmarktech.com/imprintstamps.

(21) D. Qin, Y. Xia and G. M. Whitesides, *Nat. Protoc.*, 2010, **5**, 491–502.

(22) V. E. Ferry, M. A. Verschuuren, H. B. T. Li, R. E. I. Schropp, H. A. Atwater and A. Polman, *Appl. Phys. Lett.*, 2009, **95**, 223–226.

(23) D. B. Hall, P. Underhill and J. M. Torkelson, *Polym. Eng. Sci.*, 1998, **38**, 2039–2045.

(24) J. D. Jackson, *Classical Electrodynamics*, Wiley, New York, 1998.

(25) Z.-Y. Li and L.-L. Lin, *Phys. Rev. E*, 2003, **67**, 046607.

(26) R. Biswas, S. Neginhal, C. G. Ding, I. Puscasu and E. Johnson, *J. Opt. Soc. Am. B*, 2007, **24**, 2589–2596.

(27) R. Biswas, C. G. Ding, I. Puscasu, M. Pralle, M. McNeal, J. Daly, A. Greenwald and E. Johnson, *Phys. Rev. B*, 2006, **74**, 045107.

(28) Documentation on compilation options at www.nersc.gov.

(29) E. D. Palik, *Handbook of Optical Constants of Solids*, Academic Press, San Diego, 1998.

(30) M. G. Moharam and T. K. Gaylord, *J. Opt. Soc. Am.*, 1982, **72**, 1385-1392.

(31) M. G. Moharam and T. K. Gaylord, *J. Opt. Soc. Am. A*, 1986, **3**, 1780-1787.

(32) V. Liu and S. Fan, *Comput. Phys. Commun.*, 2012, **183**, 2233–2244.

(33) J. D. Kraus, *Electromagnetics*, McGraw-Hill, New York, 1992.

(34) X. Zhang, Y. Yu, J. Xi, Y. Wang and X.-H. Sun, *J. Opt.*, 2015, **17**, 75901.

(35) M. Airola, Y. Liu and S. Blair, *J. Opt. A*, 2005, **7**, S118–S123.

(36) J. A. H. Van Nieuwstadt, M. Sandtke, R. H. Harmsen, F. B. Segerink, J. C. Prangsma, S. Enoch and L. Kuipers, *Phys. Rev. Lett.*, 2006, **97**, 146102.

(37) M. A. Kats, R. Blanchard, P. Genevet, and F. Capasso, *Nature Mater.*, 2013, **12**, 20-24.

(38) M. Esfandyarpour, E. C. Garnett, Y. Cui, M. D. McGehee and M. L. Brongersma, *Nature Nanotech.*, 2014, **9**, 542-547.

(39) A. E. Cetin, A. F. Coskun, B. C. Galarreta, M. Huang, D. Herman, A. Ozcan and H. Altug, *Light Sci. Appl.*, 2014, **3**, e122.

(40) J. N. Anker, W. P. Hall, O. Lyandres, N. C. Shah, J. Zhao and R. P. Van Duyne, *Nature Mater.,* 2008, **7**, 442-453.

(41) A. G. Brolo, *Nature Photon.*, 2012, **6**, 709-713.

(42) Y. Lu, G. L. Liu, J. Kim, Y. X. Mejia and L. P. Lee, *Nano Lett.*, 2005, **5**, 119-124.

(43) C. T. Ertsgaard, R. M. McKoskey, I. S. Rich and N. C. Lindquist, *ACS Nano*, 2014, **8**, 10941-10946.

(44) S. Kumar, G. G. Wolken, N. J. Wittenberg, E. A. Arriaga and S.-H. Oh, *Anal. Chem.*, 2015, **87**, 11973-11977.

(45) W. Lee, Y. Kinosita, Y. Oh, N. Mikami, H. Yang, M. Miyata, T. Nishizaka and D. Kim, *ACS Nano*, 2015, **9**, 10896-10908.